JGR Solid Earth

Key Points:
- A new Three-dimensional shear wave velocity model of Northern Taiwan is constructed using Rayleigh wave H/V ratios and phase velocities
- The addition of H/V ratio measurements allows detailed shallow crustal structure to be resolved with sub-kilometer depth resolution
- The resolved fine crustal structures provide new geometrical constraints on basin formation and orogeny dynamics

ADVANCING EARTH AND SPACE SCIENCE

High-Resolution 3-D Shear Wave Velocity Model of Northern Taiwan via Bayesian Joint Inversion of Rayleigh Wave Ellipticity and Phase Velocity With Formosa Array

Cheng-Nan Liu[1], Fan-Chi Lin[2,1] , Hsin-Hua Huang[1] , Yu Wang[3], Elizabeth M. Berg[2] , and Cheng-Horng Lin[1]

[1]Institute of Earth Sciences, Academia Sinica, Taipei, Taiwan, [2]Department of Geology and Geophysics, University of Utah, Salt Lake City, UT, USA, [3]Department of Geosciences, National Taiwan University, Taipei, Taiwan

Abstract The Formosa array, with 137 broadband seismometers and ~5 km station spacing, was deployed recently in Northern Taiwan. Here by using eight months of continuous ambient noise records, we construct the first high-resolution three-dimensional (3-D) shear wave velocity model of the crust in the area. We first calculate multi-component cross-correlations to extract robust Rayleigh wave signals. We then determine phase velocity maps between 3 and 10 s periods using Eikonal tomography and measure Rayleigh wave ellipticity at each station location between 2 and 13 s periods. For each location, we jointly invert the two types of Rayleigh wave measurements with a Bayesian-based inversion method for a one-dimensional shear wave velocity model. All piecewise continuous one-dimensional models are then used to construct the final 3-D model. Our 3-D model reveals upper crustal structures that correlate well with surface geological features. Near the surface, the model delineates the low-velocity Taipei and Ilan Basins from the adjacent fast-velocity mountainous areas, with basin geometries consistent with the results of previous geophysical exploration and geological studies. At a greater depth, low velocity anomalies are observed associated with the Linkou Tableland, Tatun Volcano Group, and a possible dyke intrusion beneath the Southern Ilan Basin. The model also provides new geometrical constraints on the major active fault systems in the area, which are important to understand the basin formation, orogeny dynamics, and regional seismic hazard. The new 3-D shear wave velocity model allows a comprehensive investigation of shallow geologic structures in the Northern Taiwan.

Plain Language Summary Around 137 broadband seismometers have recently been installed with ~5 km uniform station spacing across the entire Northern Taiwan. The new array, named Formosa array, provides new opportunities in studying detailed subsurface structure associated with geological features in the areas such as basins and faults. Here we first extract coherent seismic surface waves propagating between all station pairs from ambient noise records using seismic interferometry. We then measure the propagation wave speed and the ellipticity of the ground particle motion across the entire array. By using the complimentary sensitivity of the measurements, we construct a high-resolution 3-D crustal shear wave velocity model between the surface and ~12 km depth. Our model illuminates detailed subsurface geometry of the Taipei and Ilan Basins, locations and dips of major active faults in the areas, and possible magmatic structures associated with the Tatun Volcano Group and the active geothermal area in Southern Ilan. Getting clearer images of such shallow structures are important not only to understand the geological processes in an extensional tectonic setting but also to better assess the regional geohazards.

1. Introduction

Taiwan is one of the most active orogenic belts in the world, resulting from oblique convergence between the Eurasian Plate (EP) and Philippine Sea Plate (PSP) since 4–6 Ma (Ho, 1986; Mcintosh et al., 2005; Suppe et al., 1987; Teng, 1996). Through oblique collision followed by post-collisional extension, Northern Taiwan experienced intense tectonic and magmatic activities that produced complex geological structures including the fold-and-thrust belt, the onshore and offshore volcanic groups, and the post-collision extension basins (Figure 1b). Within these tectonic features, the arcuate-shaped fold-and-thrust belt in Northern Taiwan,
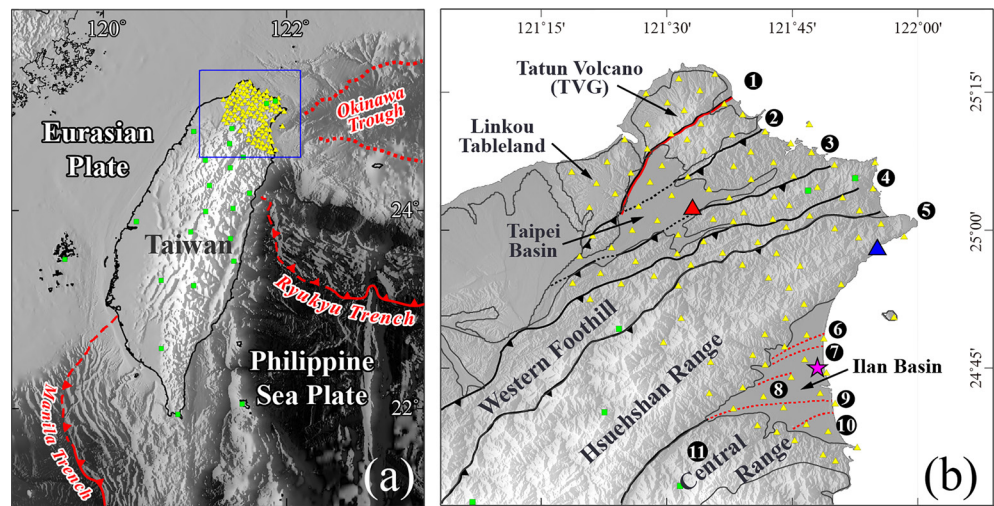
Figure 1. The tectonic map of Taiwan and seismic stations used in this study. (a) The large-scale tectonic structure of Taiwan region. BATS and FA broadband stations used are denoted as green rectangles and yellow triangles, respectively. Blue rectangle outlines the Northern Taiwan area shown in (b) which is the targeted area of this study. (b) The detailed geological structure of Northern Taiwan. Example stations CT08 and KM02 used in Figures 2 and 4 are identified by the red and blue triangle, respectively. Purple star marks the location of example 1D inversion shown in Figure 6. Number 1 to number 11 denote the known fault systems in Northern Taiwan: (1) Sanchiao Fault (SCF); (2) Kanjiao Fault (KJF); (3) Taipei Fault (TF); (4) Hsintien Fault (HTF); (5) Chuchih Fault (CCF); (6) Yaichein Fault (YCF); (7) Ilan Fault (IF); (8) Kengssu Fault (KSF); (9) Choshui Fault (CSF); (10) Sansing Fault (SSF); and (11) Lishan Fault (LSF). Faults in red and black represent active and non-active faults, respectively.

including the Hsuehshan Range and the Western Foothills, is mainly composed by the Tertiary sedimentary rocks with limited exposure of slate and argillite at the eastern flank of the belt. The Hsuehshan Range and the Western Foothills are deformed and uplifted by a series of northwest-verging thrust faults caused by the southward-propagated arc-continent collision process, with Pleistocene lateritic alluvial fan and foreland basin (e.g., Linkou Tableland; Figure 1b) developed west of the foothills (e.g., Lin & Watts, 2002; Suppe, 1981; Teng, 1996). Part of this well-developed fold-and-thrust mountain belt has subsequently been mantled by the late-Pleistocene Volcanic Rocks including the andesitic lava flow and the pyroclastic flows (e.g., the Tatun Volcano; Figure 1b). The fold-and-thrust belt is also truncated by a series of NE-SW running normal faults and extension basins, when the tectonic environment of Northern Taiwan transits from the collisional environment to the post-collisional extension environment within the past 1 Ma (Teng, 2001).

One of the major extension basins in Northern Taiwan is the Taipei Basin, where the capital city of Taiwan is built on. In contrast to its surrounding fold-and-thrust mountain belt, this triangular-shaped basin is filled with approximately 700 meters thick unconsolidated Quaternary alluvial-lacustrine deposits (Teng et al., 2001; Wang et al., 2004). The low shear-wave velocities of the sediment amplify the ground motions excited by regional earthquakes and increase the risk of seismic hazard. The 1999 M_W 7.6 Chi-Chi earthquake (Lee et al., 2007) and the 1986 M_L 6.5 and 2002 Mw 7.0 Hualien offshore earthquakes (Chen, 2003; Tsai et al., 1986), for instance, caused considerable damage to the Taipei metropolitan area due to the basin-amplified ground shaking. Another major extension basin in Northern Taiwan is the Ilan Basin, which is created by the westward extension of the Okinawa Trough along the back-arc of the Ryukyu Trench (Hou et al., 2009; Huang, Gung et al., 2012; Lee et al., 1980; Letouzey & Kimura, 1986). Previous geophysical and geological investigations suggest the normal-fault bounded Ilan Basin is filled with alluvial deposits. The maximum thickness of the alluvial deposit could reach ~1.2 km beneath the present alluvial surface (Bao et al., 2019; Chang et al., 2010; Chiang, 1976).

The on-going post-collisional extension process has also created several major active normal faults in Northern Taiwan (Teng et al., 2001). The existence of these active normal faults poses a significant seismic hazard to the densely populated Taipei metropolis and the Northern Taiwan region in general (Chen et al., 2014; Huang et al., 2007; Lai et al., 2009). For example, the southeast-dipping Shanchiao Fault at the western edge of the Taipei Basin, extending northeastward and cutting through the Tatun Volcano Group (TVG), is

capable of generating Mw ∼7.0 earthquake beneath Taipei metropolis (Shyu et al., 2005, 2016). The Lishan Fault that separates the Hsuehshan Range's slate belt and the Central Range's metamorphic core complex may also have reactivated and developed a series of active normal faults running through the Ilan Basin (Kang et al., 2015; Lee et al., 1997) (Figure 1b). A better illumination of these shallow crustal structures is of great interest to not only further understand regional tectonics but also help better assessing regional seismic hazards.

Previous attempts of such structural explorations in Northern Taiwan have mostly been made by body-wave tomographic imaging (; Kuo-Chen et al., 2012; Wu et al., 2007), seismic reflection/refraction experiments (Liu et al., 1997; Wang et al., 2004), and geological borehole investigations (e.g., Huang et al., 2007; Teng et al., 2001). However, the former lacks resolution in the uppermost crust and the latter two are largely restricted to two-dimensional profiles or specific sites in limited areas. With the recent development, ambient noise tomography, which extracts short period surface wave signals from seismic noise cross-correlations, has become a common tool to resolve shallow crustal structures (Bensen et al., 2007; Berg et al., 2018; Lin et al., 2008; Shapiro et al., 2005; Spica et al., 2018; Wang et al., 2020). While several studies have already utilized ambient noise tomography to study crustal structure across Taiwan (Huang et al., 2010, 2015; Huang, Shyu, et al., 2012), the uppermost crustal structure remains poorly resolved due to sparse broadband stations and the limited period range of surface wave dispersion measurements in the past.

Benefit from the recent Formosa Array (FA) project (Institute of Earth Sciences, Academia Sinica, 2017), about 140 broadband seismic stations were deployed across the entire Northern Taiwan with ∼5 km station spacing (Figure 1), providing an unprecedented station coverage and high-quality three-component broadband data. In this study, we first calculate multi-component noise cross-correlations between all FA stations and stations from the Broadband Array in Taiwan for Seismology (BATS; Institute of Earth Sciences, Academia Sinica, 1996) to extract short period Rayleigh wave signals. We then apply Eikonal tomography (Lin et al., 2009) to measure phase velocities across the FA array. In addition to phase velocities, for each FA station, we also measure Rayleigh wave ellipticity, in the form of horizontal-to-vertical (H/V) amplitude ratios, to enhance the imaging resolution at shallow depths (Berg et al., 2020; Li et al., 2016; Lin et al., 2014; Muir & Tsai, 2017). Combining the phase velocity and ellipticity measurements of Rayleigh waves, we perform Markov chain Monte Carlo (MCMC) joint inversion (Shen et al., 2013; Shen & Ritzwoller, 2016) at each station location to construct a high-resolution three-dimensional (3-D) shear wave velocity (Vs) model across Northern Taiwan for crustal structure investigation.

2. Data and Methods

2.1. Data

We download 8 months of three-component continuous waveform data between January 2019 and August 2019 from two broadband seismic networks, FA and BATS (Institute of Earth Sciences, Academia Sinica, 1996, 2017). Since data from few mountainous FA stations was not available at the time when we conducted this research, a total of 137 stations were used in the end (Figure 1). The inclusion of BATS stations provides few longer ray paths and allows us to study the longer period surface waves, which are essential to constrain slightly deeper crustal structure.

We follow closely to the method described by Bensen et al. (2007) to preprocess the daily noise records. To only include the high quality data, we exclude daily records with time series shorter than 60,000 s. We remove the instrument response, mean, and trend from the daily waveforms and decimate them to a 5 Hz sampling rate. To retain the relative amplitude information between different components, for each station, we simultaneously normalize the three-component records following the process described by Lin et al. (2014). First, we filter the waveforms between 15 and 50 s period to extract the most energetic earthquake signals and calculate the temporal normalization function for each component based on the 128-s time window running absolute mean. For each point in time, we divide the three-component unfiltered daily waveforms by the maximum of the three-component temporal normalization functions to suppress the undesired energetic signals. To equalize the power at all frequencies, we then apply spectral whitening for each component using the averaged smoothed spectrum of the three components. We cross-correlate the temporal and spectral normalized waveforms and stack them to obtain the final nine-component cross-correlation
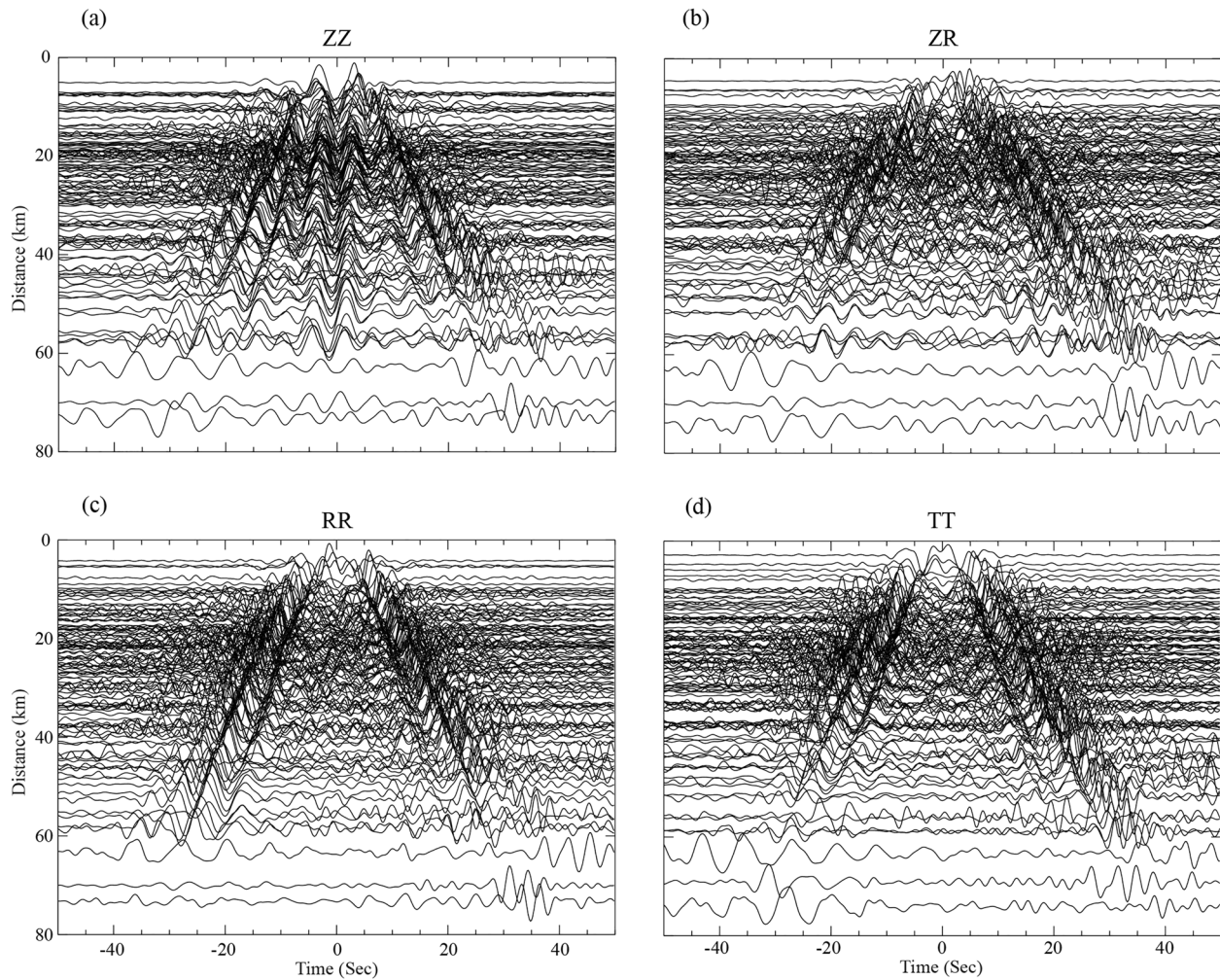
Figure 2. Example cross-correlation record sections. (a)–(d) are all 4 components (ZZ, ZR, RR, and TT) cross-correlations band passed between 2 and 10 s period with CT08 (red triangle in Figure 1b) as the common source station. Note that the record section of the RZ component, which is not shown, is very similar to the ZR component. (a–c) The cross-correlations of ZZ, ZR, RR, RZ are the components with the information of Rayleigh wave we analyzed in this work. (d) The cross-correlations of TT show the information of Love wave.

functions (ZZ, ZN, ZE, NN, NE, NZ, EE, EN, and EZ) between each station pair. Using a rotation matrix (Lin et al., 2008, 2014), we convert the horizontal components and obtain the rotated cross-correlations (RCORs) in radial (R) and transverse (T) directions. Example cross-correlation record sections are shown in Figure 2, where both Rayleigh (Figures 2a–2c) and Love wave (Figure 2d) moveouts can be clearly observed. While in principle both Rayleigh and Love wave measurements can be made (Lin et al., 2008), we will only focus on analyzing Rayleigh wave signals and constructing the first high-resolution isotropic Vs model for Northern Taiwan in this study. Using directional-dependent surface wave measurements (Feng et al., 2020; Lin et al., 2011; Yao et al., 2010) and Rayleigh-Love discrepancy (Jaxybulatov et al., 2014; Jiang et al., 2018; Moschetti et al., 2010) to investigate anisotropy can reveal important information about crustal deformation but will be the subject of future studies.

2.2. Rayleigh Wave Phase Velocity

We follow closely to the Eikonal tomography method described by Lin et al. (2009) to obtain Rayleigh wave phase velocity maps between 3 and 10 s period. To enhance the surface wave signals for travel time measurement, we fold and stack the ZZ correlation functions before we apply frequency-time analysis to obtain Rayleigh wave phase velocity dispersion curves (Bensen et al., 2007; Lin et al., 2008). We calculate the period
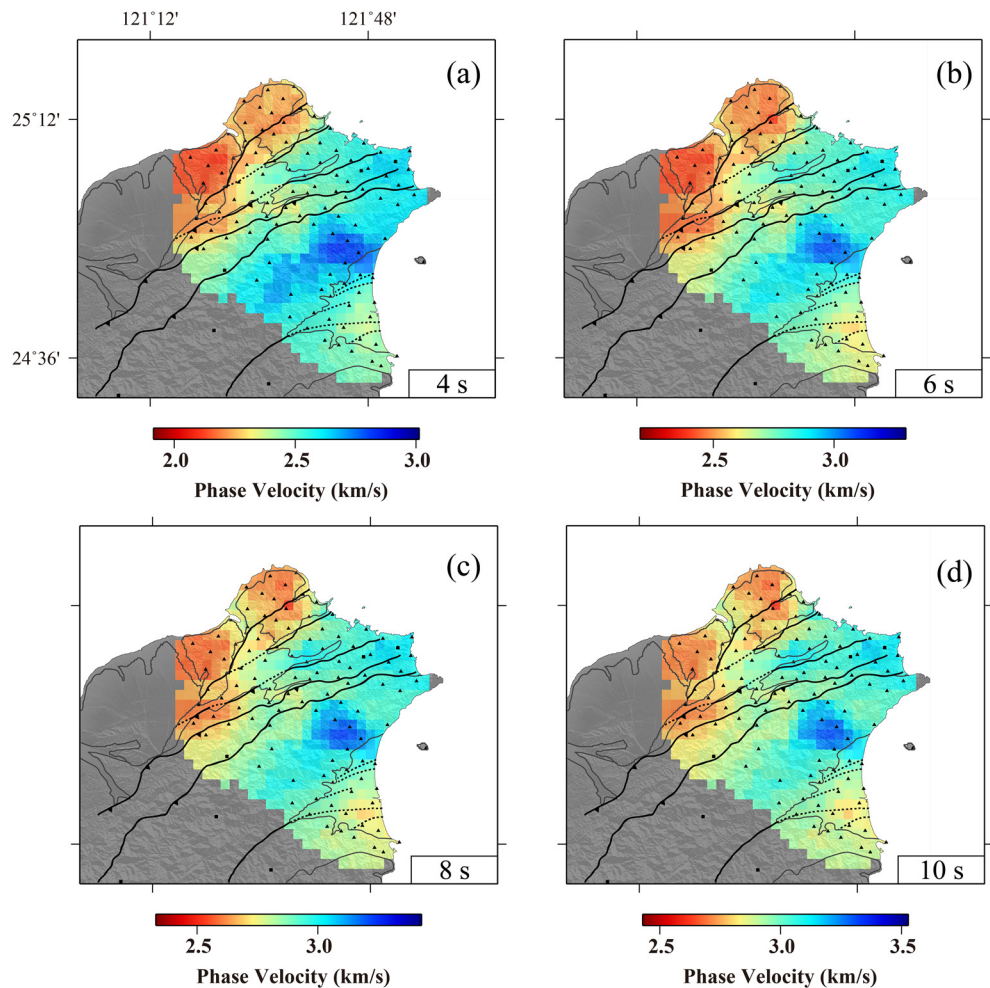
Figure 3. Rayleigh wave phase velocity maps. (a) Rayleigh wave phase velocity map at 4 s period constructed using Eikonal tomography. (b)–(d) Same as (a) but for 6, 8, and 10 s periods.

dependent signal-to-noise ratio (SNRs) for each cross-correlation, where SNR is defined as the ratio between the maximum amplitude within the signal window (determined by the minimum reference velocity of 1.5 km/s and maximum reference velocity of 4.5 km/s) and the root-mean-square amplitude of noise following the signal window. All measurements with SNR < 8 or with distance shorter than a wavelength are removed from further analysis. For each period, we consider each station as a virtual source and all phase travel time measurements with that source station in common are interpolated to construct a phase travel time map with 0.025° by 0.025° grid spacing. We employ phase front tracking to correct for potential 2-pi jumps and remove measurements that are not consistent with nearby stations (Lin et al., 2009). By solving the Eikonal equation, for each map and each grid point, we determine the local apparent phase slowness (i.e., the inverse of phase velocity) and the direction of wave propagation using travel time gradient. Stations at locations with travel time curvature above 0.3 s/km^2 are removed. Slownesses with value outside of 0.2 and 0.7 s/km or without at least three of the four quadrants occupied by at least one station within 10 km are discarded. For each grid point, we take the mean and the standard deviation of the mean of all available measurements from different virtual sources to determine the final phase velocity and its uncertainty. To only include the most reliable measurements, we remove measurements that are outside of 1.5 standard deviations. The examples of the derived phase velocity maps are shown in Figure 3.
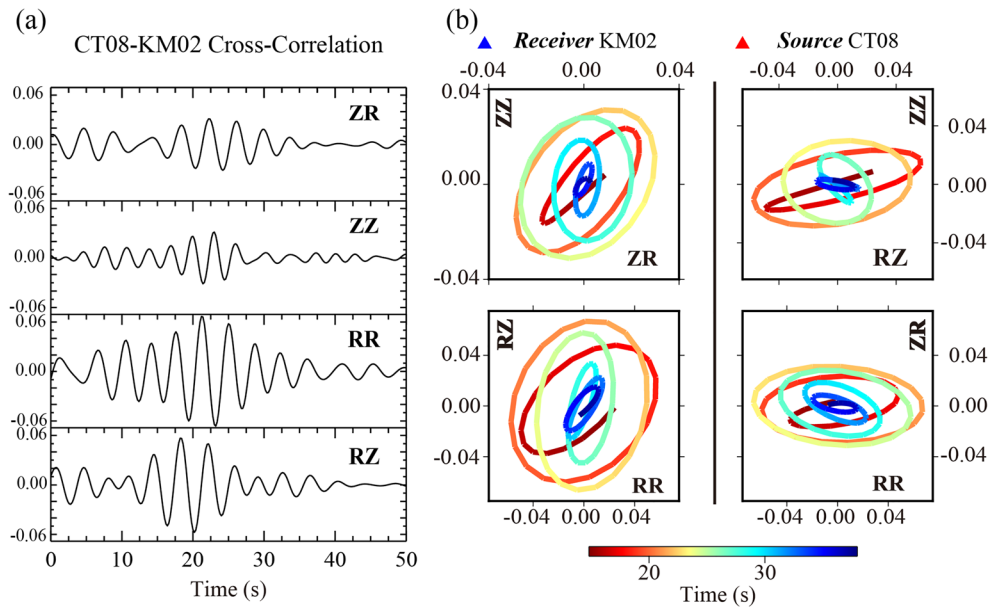
Figure 4. Rayleigh wave H/V ratio measurements between CT08 and KM02 stations. (a) Four component (ZR, ZZ, RR, RZ) cross-correlations (positive lag) between CT08 (source station; red triangle in Figure 1b) and KM02 (receiver station; blue triangle in Figure 1b) at 4 s period. (b) Rayleigh wave particle motions at CT08 (left panels) and KM02 (right panels) constructed by the combination of four cross-correlations (ZR, ZZ, RR, RZ) with KM02 and CT08 acting as the virtual source, respectively.

2.3. Rayleigh Wave Ellipticity

We follow the process described in Lin et al. (2014) and Berg et al. (2018) to determine Rayleigh wave ellipticity, or the H/V amplitude ratio, between 2 and 13 s period using the vertical and radial cross-correlation functions (Figure 2). For each period and each station pair, we obtain the H/V ratios at the first station (source station) by taking the amplitude ratio between the RZ and ZZ RCORs as well as the RR and ZR RCORs. Here, we process the positive and negative components separately such that a maximum of four independent measurements can be obtained (Berg et al., 2018). For the second station (receiver station), we use the amplitude ratios between ZR and ZZ RCORs and the RR and RZ RCORs instead (Figure 4). Multiple quality controls are imposed, including SNR ≥ 5, station spacing larger than a wavelength, and excluding the measurements larger than three standard deviations, to remove unreliable measurements. For each period and station, the mean and standard deviation of the mean for all measurements using different station pairs are used to determine the final H/V ratio and its uncertainty. For each period, to obtain the H/V ratio map with 0.025° by 0.025° grid spacing, we smooth the H/V ratios using a 5 km width Gaussian weighted function. Figure 5 shows the H/V maps at four example periods.

2.4. Monte Carlo Joint Inversion

To obtain a one-dimensional (1-D) Vs velocity model at each grid, we use the MCMC Bayesian inversion procedure described by Berg et al. (2018) to jointly invert period dependent phase velocity and H/V ratio measurements. Instead of producing one single minimum misfit model, the MCMC inversion produces an ensemble of acceptable models that can be used to quantify model uncertainties and tradeoff between different parameters (Roy & Romanowicz, 2017; Shen et al., 2013). The parameters used for MCMC inversions are summarized in Table 1. To construct a reference 1-D Vs reference model (m0), we take the 1-D averaged Vs model of Huang et al. (2014) between 2 and 35 km depth, combined with a generic 2 km thick sedimentary layer on the top with Vs increasing linearly from 1 km/s to 3 km/s. In addition to three parameters describing the linear sedimentary layer, we prescribe the shear velocity model between 2 and 35 km depth by 6 cubic B-splines (Table 1). We determine the Vp and density using the empirical relationship described by Brocher (2005). Owing to the relatively short periods (<13 s) of our measurements, a homogeneous half
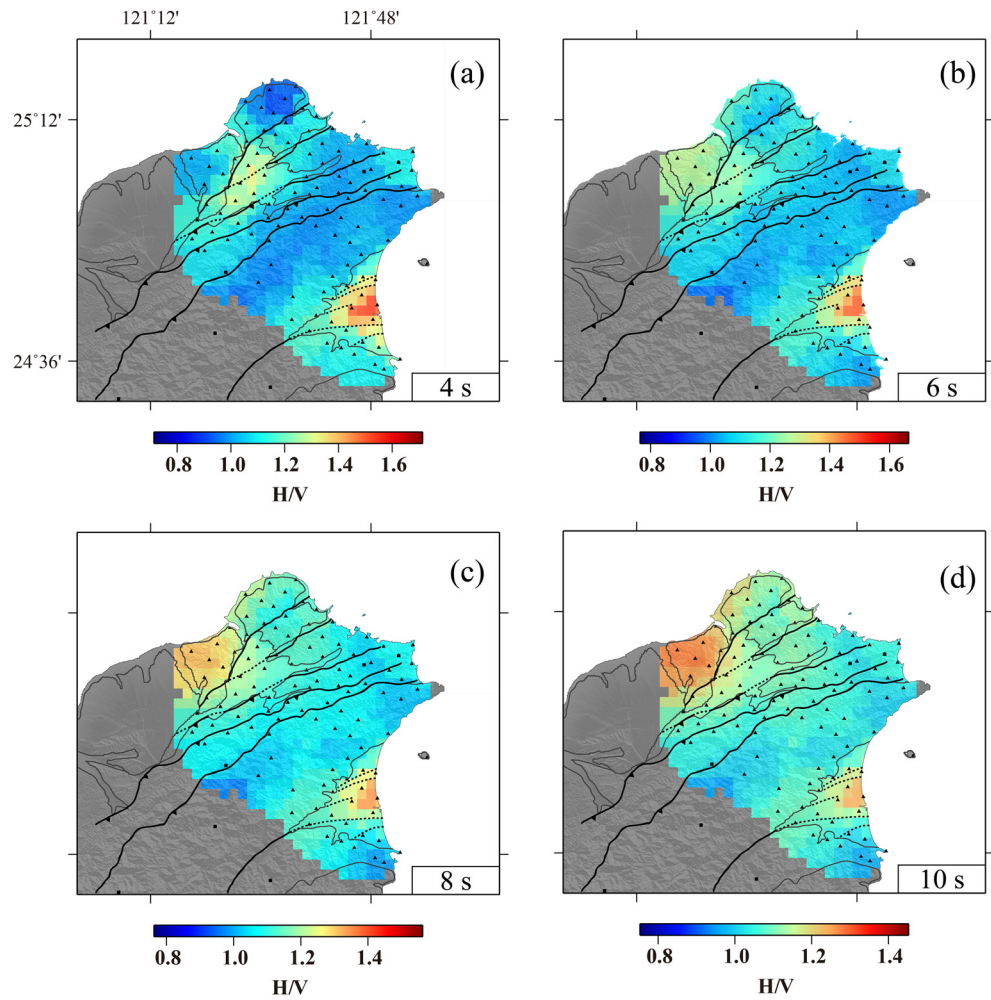
Figure 5. Smoothed Rayleigh wave H/V ratio maps. (a) The smoothed Rayleigh wave H/V ratio map at 4 s period. (b)–(d) Same as (a) but for 6, 8, and 10 s periods.

space model is assumed below 35 km depth. Several criteria are imposed on the inversion to stabilize the inversion performance, which include: (1) the maximum Vs allowed in the crust is 4.9 km/s; (2) the Vs of sedimentary layer increases with depth; and (3) velocity jump at the base of the sedimentary layer is positive. Around 3000 iterations are run to search for the minimum misfit model. To avoid being trapped in local minimums, we allow the model to jump 12 times such that model space is being searched randomly. At the end of the inversion, all models with misfits within 2.5 times of the minimum misfit are considered acceptable. We take the averaged and the standard deviation of all acceptable models as the final model and the model uncertainty. The MCMC joint inversion results, along with the phase velocity and H/V ratio measurements and posterior model distribution, at one example location within the Ilan Basin are summarized in Figure 6.

## 3. Results

3.1. Results of Phase Velocity and H/V Map

The derived phase velocity (Figure 3) and H/V ratio (Figure 5) maps show patterns that are largely consistent with the tectonic features of the Northern Taiwan (i.e., basins and fold-and-thrust mountain belt). In

Table 1
Parameters Used in MCMC Inversion

Parameter	Range	Gaussian width
Sedimentary Thickness (km)	$m_0 \pm 2.0$	0.05
Vs, top of the sedimentary layer (km/s)	$m_0 \pm 0.5\,m_0$	0.05
Vs, top of the sedimentary layer (km/s)	$m_0 \pm 0.5\,m_0$	0.05
Crust zeroth B-spline (km/s)	$m_0 \pm 0.2\,m_0$	0.05
Crust first B-spline (km/s)	$m_0 \pm 0.2\,m_0$	0.05
Crust second B-spline (km/s)	$m_0 \pm 0.2\,m_0$	0.05
Crust third B-spline (km/s)	$m_0 \pm 0.2\,m_0$	0.05
Crust fourth B-spline (km/s)	$m_0 \pm 0.2\,m_0$	0.05
Crust fifth B-spline (km/s)	$m_0 \pm 0.2\,m_0$	0.05
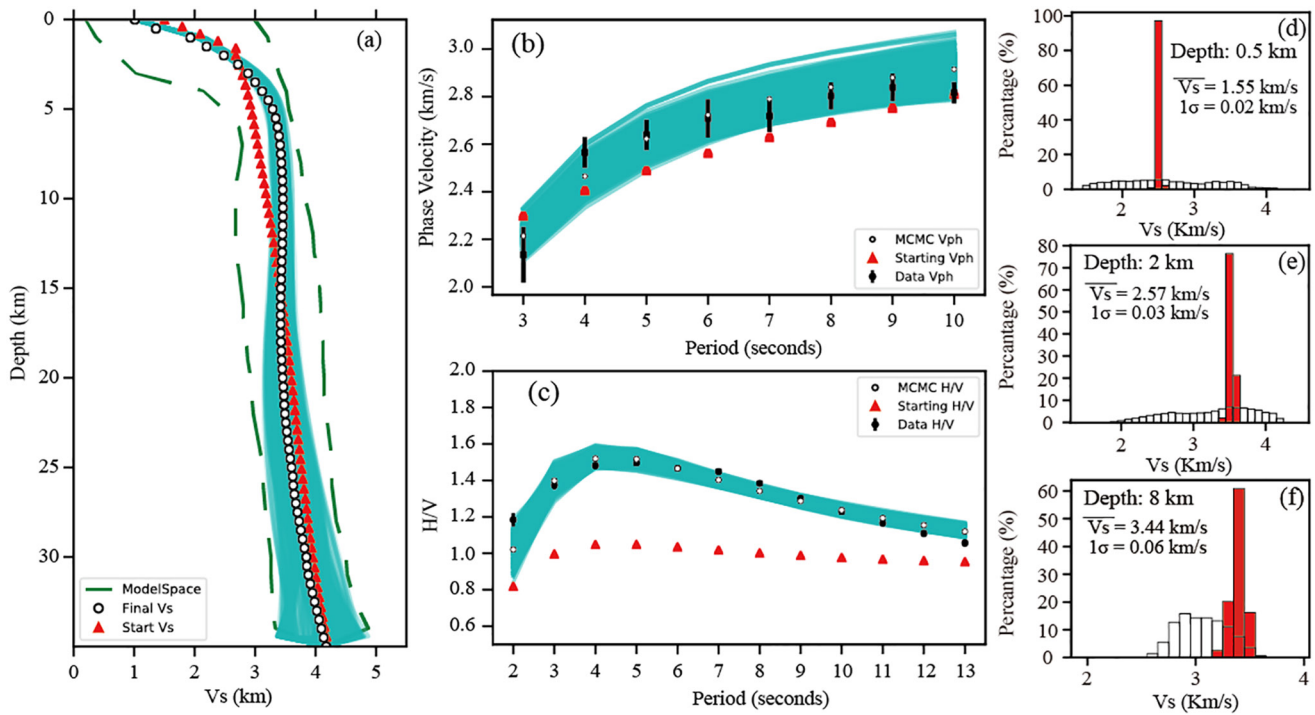
Figure 6. The 1-D MCMC joint inversion for an example location within the Ilan Basin (purple star in Figure 1b). (a) The inverted 1-D Vs profile between 0 and 35 km depth with the full searching space (green dash lines), starting model (red triangles), posterior models (cyan lines), and final 1-D model (white circles) identified. (b) The observed phase velocity dispersion with uncertainty (black dots and lines) and the phase velocity dispersions predicted from the starting model (red triangles), posterior models (cyan lines), and the final model (white circles). (c) Same as (b) but for H/V ratios. (d) The priori (transparent) and posterior (red) distribution of Vs at 0.5 km depth. The mean and standard deviation of the distribution are also shown. (e)–(d) Same as (d) but for 2 and 8 km depth.
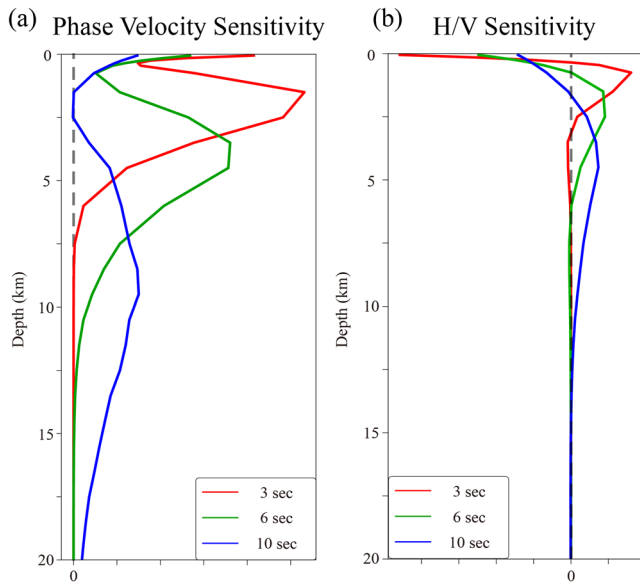

Figure 7. Sensitivity kernels for Rayleigh wave phase velocities and H/V ratios. (a) Example Vs sensitivity kernels for Rayleigh wave phase velocities at 3, 6 and 10 s period. (b) Same as (a) but for Rayleigh wave H/V ratios. The sensitivity kernels are calculated numerically through model perturbation (Tanimoto & Rivera, 2008).

general, areas with high H/V ratios and low phase velocities are correlated with major sedimentary features such as the active depositional basin (Taipei and Ilan Basins) and the Pleistocene alluvial fan (Linkou Tableland). Areas with low H/V ratios and high phase velocities are correlated with the fold-and-thrust belts including the Hsuehshan Range to the east and the Western Foothills to the west. As H/V ratios are more sensitive to near surface structure than the phase velocity at the same frequency (Figure 7), it is not surprising that our short-period H/V results provide better illuminations of the geometry of the shallow sedimentary basins. For example, our H/V measurements at 4-s clearly illustrate the shape of both Taipei and Ilan Basins, and the sharp changes of H/V ratios also aligned well with various active normal faults within these two basins (Figure 5a). At longer periods (Figures 5b–5d), the high H/V anomaly associated with the Taipei Basin becomes less apparent as the longer period H/V ratios are sensitive to slightly deeper structures. As both Ilan Basin and Linkou Tableland are thicker/deeper sedimentary features, the two features remain prominent in longer period phase velocity and H/V ratio maps. With the deeper sensitivity in general, the phase velocity maps (Figure 3) not only illuminate major sedimentary features but also better resolve deeper tectonic features such as the boundary between the Western Foothills and the Hsuehshan Range.

We note that the low H/V ratios are observed at the TVG (Figure 5), particularly at short periods north of the Shanchaio Fault. This low H/V ratio area is geographically correlated to the volcanic rocks sourced from the
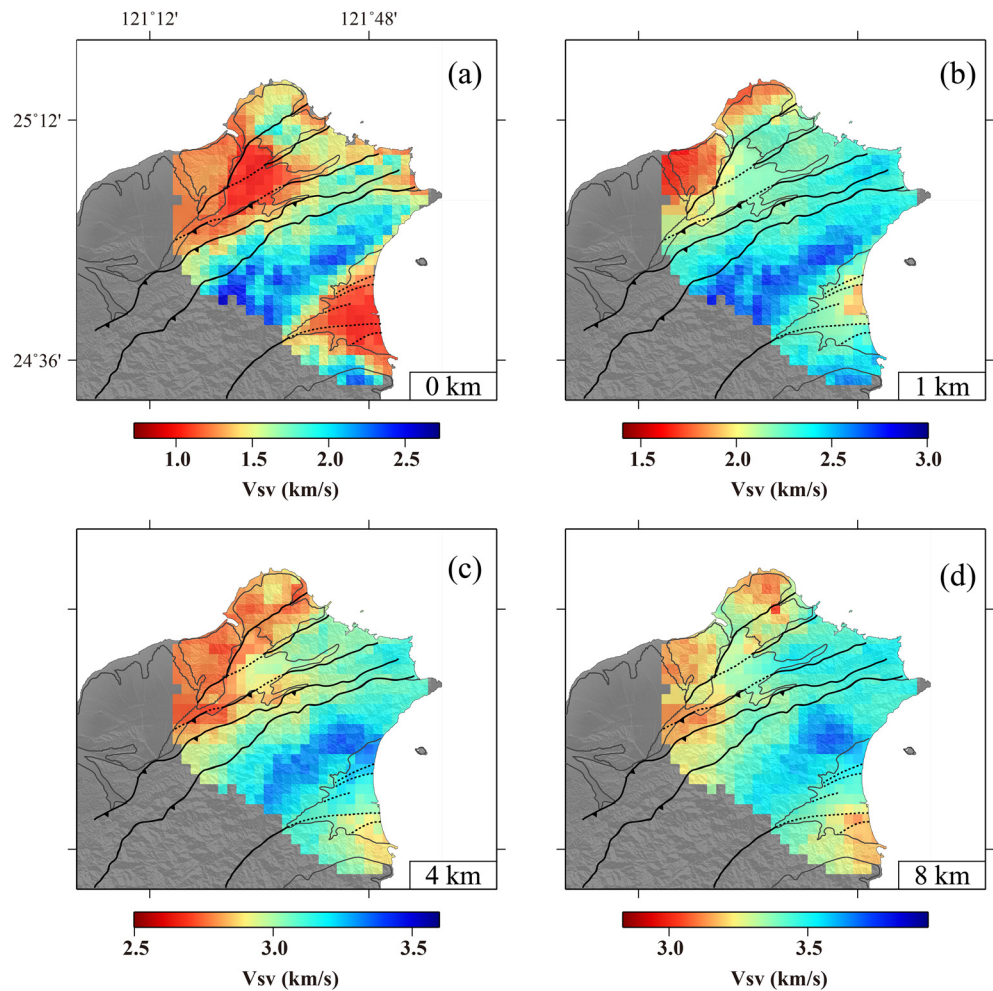
Figure 8. The shear wave velocity (Vs) of the final inverted model. Depth slices at (a) 0 km, (b) 1 km, (c) 4 km, (d) 8 km depth.

Chutzeshan Volcano Subgroup, likely corresponding to the several hundred meter thick high-velocity igneous rocks (e.g., Lava flow) formed at the northern part of the Tatun Volcano (Teng et al., 2001).

3.2. MCMC Inversion Results

The MCMC joint inversions in general produce models that can explain the observed Rayleigh wave phase velocity dispersions and H/V ratios across the North Taiwan (e.g., Figures 6b and 6c). Benefit from the complimentary sensitivity of phase velocity and H/V ratio measurements (Figure 7), confined posterior model distribution is obtained above about 12 km depth (Figures 6d–6f), while the posterior model distribution broadened considerably below 12 km depth (Figure 6a) due to the lack of long period measurements. Considering the increased uncertainty of our model at the greater depth, we will only discuss features presented in our model above 12 km depth, which are considered robust.

3.3. 3-D Shear Velocity Model

Four depths (relative to sea level) of the final 3-D Vs model constructed by the MCMC joint inversion are shown in Figure 8 with the corresponding uncertainties shown in Figure 9. At 0 km depth, clear low velocity anomalies (< 1.0 km/s) associated with loose unconsolidated sediments within the triangular Taipei and Ilan Basins are observed (Figure 8a). Slightly higher, but still slow, velocities are also observed beneath the Linkou Tableland, reflecting the better consolidated Pleistocene conglomerate and sandstone formations
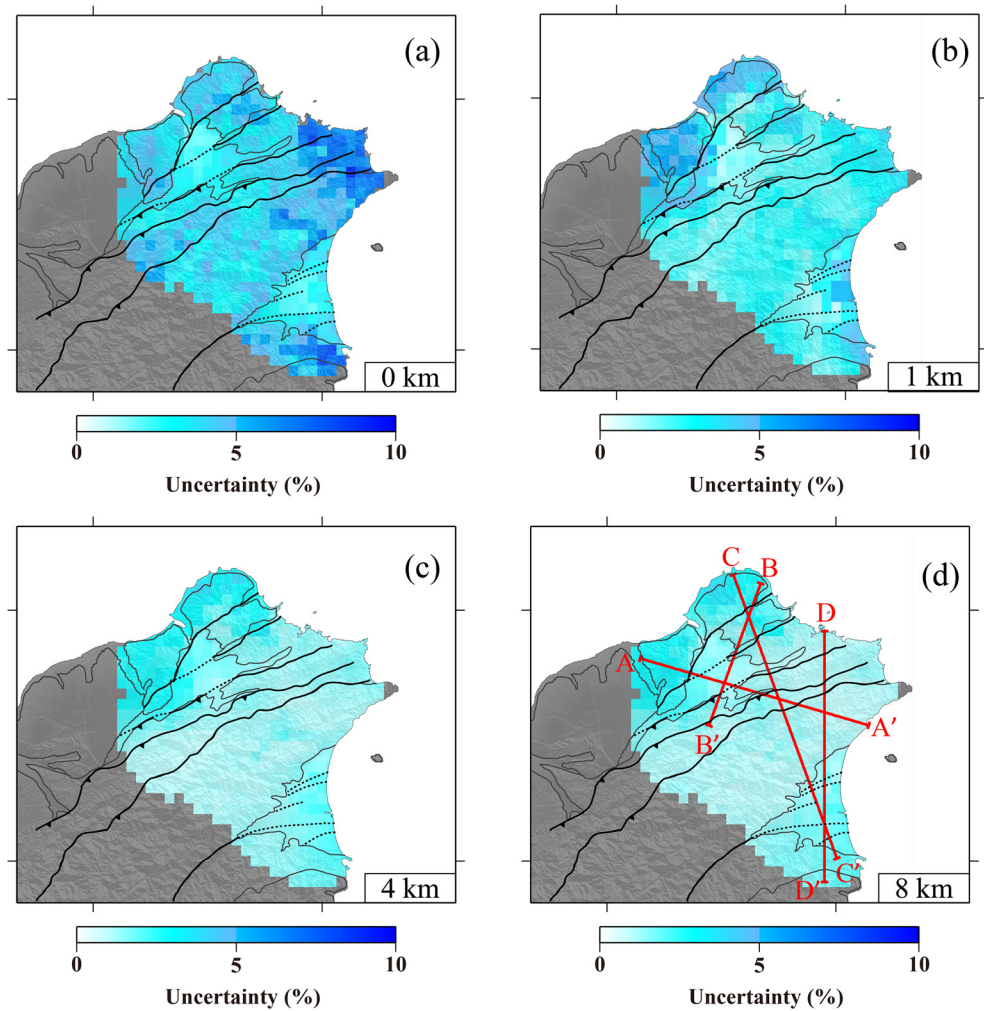
Figure 9. The Vs uncertainty of the final inverted model. Depth slices at (a) 0 km, (b) 1 km, (c) 4 km, (d) 8 km depth. Red lines in (d) denote the cross-section profiles shown in Figure 10.

near the surface. High velocities, on the other hand, are observed along the Hsuehshan Range, especially along the eastern flank of the range, correlated with the metamorphic slate and argillite belt exhumed during the mountain building process. A small but noticeable high velocity anomaly can be found at the center of the TVG, associated to the high-velocity lava flow from the Tatun Volcano.

At 1 km depth (Figure 8b), while major features are similar to the velocity structure at the surface, the Taipei Basin is no longer well pronounced. Instead, the velocity beneath Taipei becomes similar to the velocity in the Western Foothill. Previous studies (e.g., Teng et al., 2001; Wang et al., 2004) determined the contact between the unconsolidated basin sediment and the Tertiary sedimentary basin floor is about 680 m depth at the deepest part of the Taipei Basin; such observation is supported by our velocity map at the 1 km depth. In contrast, the Vs in the Ilan Basin remains slow at this depth particularly in the area bounded by the Choshui Fault and other normal faults along the northern margin of the Ilan Basin. This suggests the sedimentary deposition of the Ilan Basin and its basin geometry are likely controlled by these active normal faults beneath the basin.

At 4 km depth, the Linkou Tableland remains as a pronounced low velocity feature. It is also clear that the boundary between the high-velocity and low-velocity, extended from the northern coast of the Tatun Volcanos to the eastern margin of the Linkou Tableland, retreats southeastward from the 1-km depth slice to the 4-km depth slice. The change of velocity boundary position matches to the northwest-verging thrust fault developed in the fold-and-thrust belt, before the inactive thrust fault reactivated as the normal Shanchiao

Fault in the past 1 Ma. In contrast to a fast anomaly observed in the top 1 km slice, TVG shows up as a slow anomaly at this depth revealing the sedimentary formation capped beneath the igneous rocks (Teng et al., 2001).

At 8 km depth, the slow velocity anomaly observed beneath the TVG is likely related to the magmatic structure beneath the volcano. A low velocity anomaly is also observed in the southern Ilan Basin where a high level of geothermal activities and seismicity is present (Huang, Gung et al., 2012; Lai et al., 2009). It is intriguing to note that the northern bound of this slow anomaly somewhat coincides with the Choshui Fault, the seaward extension of the Lishan Fault (Kang et al., 2015). It is also worth noticing that the high velocity anomaly associated with the Hsuehshan Range seems to turn slightly toward the southeast and occupy the northern part of the Ilan Basin beneath ∼4 km depth (Figures 8c and 8d).

Except for the northeastern tip of Taiwan at surface (Figure 9a) and the western coast at 1 km depth (Figure 9b), velocity uncertainties are well below 3%–4%. We estimate our model to have a lateral resolution around ∼5 km similar to the average station spacing of the FA based on previous studies with similar nature (Lin et al., 2009; Lin et al., 2014)

4. Discussion

Four selected cross-sections are shown both in absolute Vs and velocity perturbations to better illustrate and explore major geological structures in the Northern Taiwan (Figure 10). The velocity perturbations are calculated relative to the average velocity at each depth from sea level. For reference, the corresponding model uncertainties for the four cross-sections are shown in Figure 11. We note that the slightly higher percentage uncertainty near the surface mostly reflects the tradeoff between shallow Vs and the thickness of the sedimentary layer where both parameters are allowed to vary freely in the inversion.

4.1. Taipei Basin and Shanchiao Fault

During the late-Quaternary post-collisional extension of the northern mountain belt, the half-graben shape Taipei Basin was formed by successive slips of the reactivated high-angle normal Shanchiao Fault to the west (Chen et al., 2007, 2014;; Teng et al., 2001). Abundant sedimentary records have been compiled by borehole data in the Taipei Basin, suggesting the maximum sediment thickness at the western part of the basin reaches ∼680 m, at a place close to the Shanchiao Fault-line scarp (Wang et al., 2004). Wang et al. (2004) also conducted over 300 shallow reflection seismic lines across the basin, incorporating with the borehole data, to investigate the seismic properties of the sedimentary formations and basement. Their result shows that the P-wave and S-wave velocities within the formations range between 1500–2200 m/s and 170–880 m/s, respectively, and are 3000 m/s and 1500 m/s for the Tertiary sedimentary rocks beneath the basin floor.

In our model, the cross-section AA′ clearly shows the half-graben geometry of the Taipei Basin, particularly in velocity perturbations, bounded by the steep Shanchiao Fault to the west and a gentle west-dipping basin floor to the east (Figure 10a). Assuming 1500 m/s S-wave velocity for the Tertiary sedimentary rocks below the basin, the deepest part of the Taipei Basin is around 700 m deep. This excellent agreement between our model and the result of previous studies (Teng et al., 2001; Wang et al., 2004) demonstrates the outstanding shallow sensitivity of the H/V ratio measurements (Figure 7b). It is important to note that the model inverted with H/V ratios significantly help to resolve the basin geometry. By comparing the cross-section extracted from models inverted with only phase velocity measurements (Figure S1), we find the phase velocity-only inversion could reveal low velocity anomaly associated with the Taipei Basin, yet the geometry of the basin is poorly resolved. Thus, it is important to combine both the phase velocity and the H/V ratios to resolve shallow crustal structures, especially the geometry of active sedimentary basins. Several studies have pointed out the importance of unconsolidated sediments and basin geometry to site response and ground motion amplification (Chen et al., 2020; Lee et al., 2008; Olsen, 2000; Smith & Tape, 2019). A high-resolution 3-D basin model constructed using both the phase velocity and the H/V ratio hence may play a critical role in the seismic hazard assessment.

Other than the geometry of the Taipei Basin, our A-A′ profile also suggests a thick layer (∼2 km) of low-velocity sedimentary rocks beneath the Linkou Tableland (Figure 10a). The velocity boundary between the
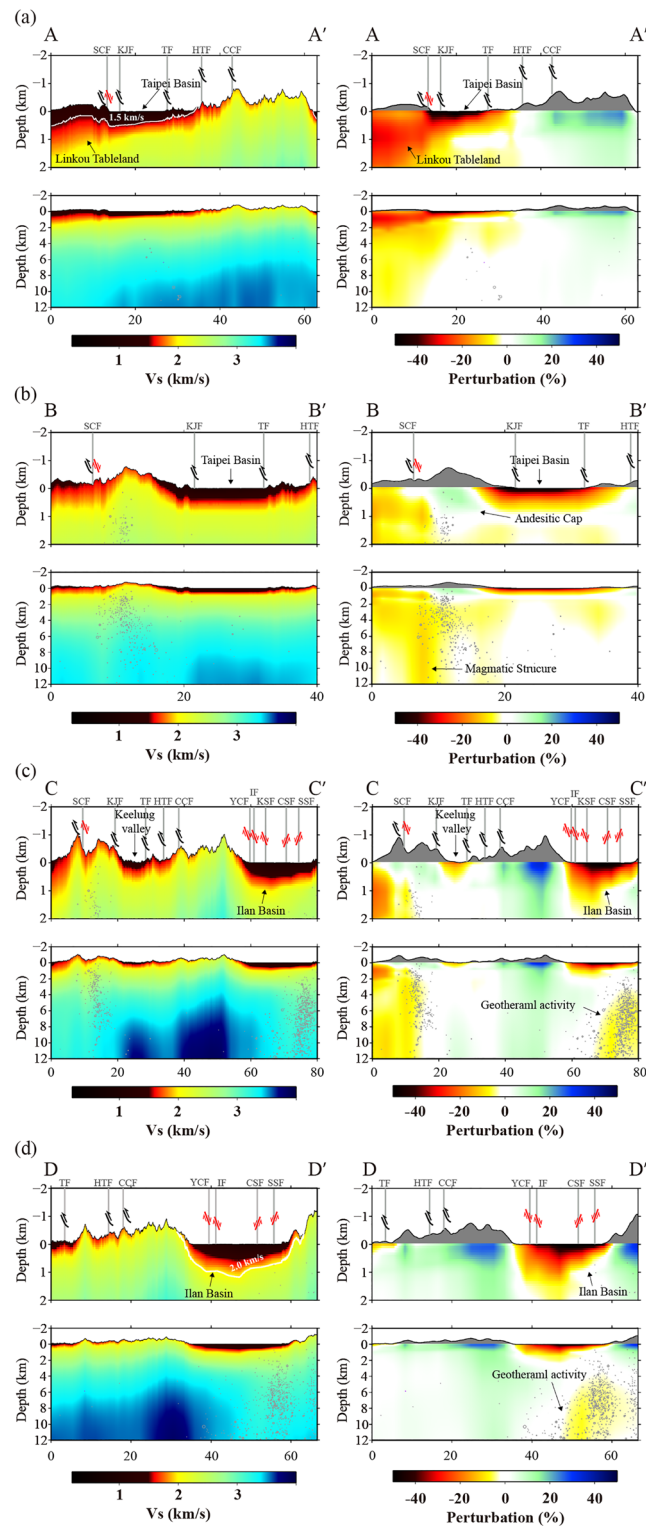
Figure 10. Cross sections of Vs (left) and Vs perturbation (right) along A-A′, B-B′, C-C′, and D-D′ profiles (Figure 9d). Gray lines mark the fault system shown in Figure 1b. (a) A-A′ cuts through the extension profile of Teng et al. (2001). From west to east, it cuts through the Guanyin Mountain, Sanchiao Fault, Taipei Basin and the northeast part of the Hsuehshan Range. (b) B-B′ cuts through the Tatun Volcanic Group and Taipei Basin. (c) C-C′ cuts through the Tatun Volcanic Group, Hsuehshan Range, Ilan Basin, and hydrothermal active area in Southern Ilan. (d) D-D′ cuts through the Hsuehshan Range, Ilan Basin, and hydrothermal active area in Southern Ilan. The red and black arrows indicate the shearing sense of active and non-active faults. Gray dots are the relocated seismicity from Huang et al. (2021).
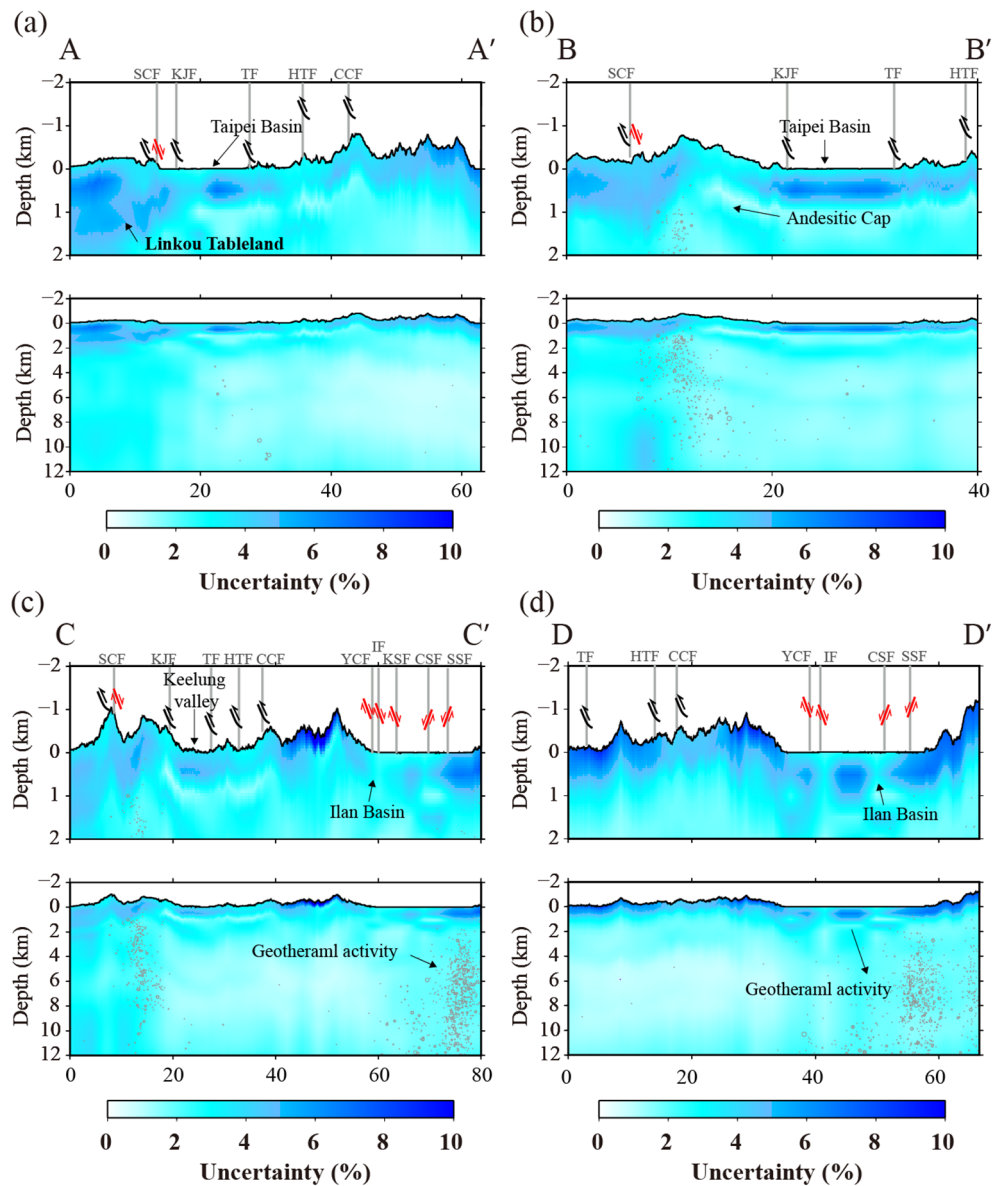
Figure 11. Cross sections of uncertainty along (a) A-A′, (b) B-B′, (c) C-C′, and (d) D-D′ profiles (Figure 9d). Gray dots are the relocated seismicity from Huang et al. (2021).

Linkou Tableland and the Taipei Basin (fast to slow near the surface but slow to fast at below 1 km depth) also matches the location of Shanchaio Fault, which seems to dip southeastward in the perturbation profile. Both the location and the dip-direction suggest the Shanchaio Fault controls the velocity offset. Previous geological studies along the Shanchaio Fault suggest this active normal fault is reactivated from a pre-existing thrust fault that separates the fold-and-thrust mountain belt to the east and the undeformed foreland basin to the west (Huang et al., 2007; Suppe, 1980). Under the Linkou Tableland, Lin and Watts (2002) also suggests the sediment thickness of the undeformed foreland basin is about 2 km, coinciding with the thickness of the low velocity layer indicated by our model. East of the Taipei Basin, high velocity anomalies are observed beneath the fold-and-thrust belt, likely corresponding to the exhumation of deeper rocks (Suppe, 1980).

4.2. Tatun Volcano Group

The profile B-B′ and C-C′ show velocity structure associated to the TVG, which is the volcano complex consisting of more than 20 andesitic edifices of Pliocene-Pleistocene age (Figures 10b and 10c). While the TVG's early eruptions may trace back to 2.8–2.5 Ma (Wang & Chen, 1990), the major eruption phase of TVG occurred around 0.8–0.2 Ma, after the formation of the fault-and-thrust belt and the foreland basin in the Northern Taiwan (Song, 2000; Teng et al., 2001). Previous geological studies suggest the andesitic lava flow and the pyroclastic flows from TVG mantled the surrounding Tertiary sedimentary rocks, and the base of the TGV is truncated by the Shanchiao Fault since the onset of the normal faulting around 0.8 Ma.

Our NNE-SSW striking cross-section B-B′ runs through the TVG and the Taipei Basin shows a clear high velocity anomaly at 0–1 km depth beneath the TVG in both the phase velocity and the velocity perturbation plots (Figure 10b). The high-velocity anomaly is likely representing the crystallized andesitic edifice overlying the slower sedimentary rocks. This interpretation is supported by the geological investigations and borehole data, where more than 1-km thick volcanic rocks were found capping the Tertiary sedimentary rocks near the center of TVG (e.g., Chu et al., 2018). The thickness of the volcanic rocks sharply reduced northwest of the Shanchaio Fault, as the southeast dipping normal fault cuts through the TVG forming a tectonic graben in the southeast side that hosts a significant amount of TVG's volcanic rocks (Figure 10b).

At the greater depth, a confined low velocity anomaly is observed below ∼6 km depth, where seismicity tends to distribute above and on the side of the anomaly (Figure 10b). This slow anomaly might be related to the magmatic structure of the TVG. Few recent studies have presented evidence indicating the presence of a mid-crustal magma body associated with the Tatun Volcano (Huang et al., 2021; Lin, 2016). The relative shallow slow anomaly we observed might be related to the remnant magmatic materials left from previous eruptions, or part of the still active magmatic system. Resolving the connection between the upper-crustal low velocity structure presented in this study and the previous identified mid-crustal slow anomaly is out of the scope of this study but will be the focus of future investigations.

The aforementioned low-velocity anomaly below TVG is also very prominent in the NNW-SSE running cross-section C-C′ (Figure 10c). The C-C′ profile is perpendicular to the Shanchaio Fault in the north and cut through the Ilan Basin in the south (Figure 10c). In the northern part of the C-C′ profile, the high-velocity anomaly that we previously discussed in B-B′ can be also observed in this profile. The profile C-C′ not only shows the high-velocity volcanic rocks sitting on top of the low-velocity foreland sedimentary rocks, but also shows the volcanic rock thickness sharply changed across the Shanchaio normal Fault. This thickness difference between the hanging and the footwall of the active Shanchaio Fault thus suggest the TVG's volcanic rocks is offset by the active normal faulting during the formation of TVG.

4.3. Fold-and-Thrust Belt

Southeast of the TVG in the profile C-C′, a shallow low-velocity layer is found in the Keelung Valley. Since the fluvial sediments in the Keelung Valley is much thinner than sediments in the Taipei Basin (e.g., < 50 m; Teng et al., 2001), the low velocity of Keelung Valley is likely associated with both the thin Quaternary fluvial sediments in the valley as well as the syncline structure that runs parallel to the Keelung Valley, where relatively young sedimentary rocks are surrounded by older rocks of the fold-and-thrust belt.

The southeastern half of the C-C′ profile also reveals structures associated with Western Foothills and the Hsuehshan Range in addition to the Ilan Basin. Southeast of the Keelung Valley, a sharp velocity contrast can be observed in the velocity perturbation profile illustrating the Pleistocene Hsintien Fault in the Western Foothills. The Hsintien Fault is a major southeast-dipping reserves fault in Northern Taiwan. Both field observations and structural reconstructions suggest the Hsintien Fault has the characteristics of a steep fault plane and significant stratigraphic offsets (≥ 3000 m) (Huang et al., 1994; Suppe, 1980). These features match with our velocity model where deep and highly compacted sedimentary rocks in the southeast were uplifted by the Hsintien Fault, forming a sharp velocity boundary in the Western Foothills.

The velocity once again increases across the Chuchih Fault between the Western Foothills and the Hsuehshan Range. East of the Chuchih Fault, the near-surface Vs is over 2 km/s suggesting the deep buried rocks have exhumed to the surface. Our observations match with the regional geology that the low-grade

metamorphic rocks, including slate, argillites, and sandstones exposed in Hsuehshan Range (e.g., Chang & Lin, 2015). At the eastern margin of the Hsuehshan Range, the mountain range is offset by a series of southeast-facing normal faults associated with the Ilan Basin (Kang et al., 2015).

4.4. Ilan Basin

The Ilan Basin is a deltaic basin covered by massive fluvial deposits and bounded by the Huseshshan Range to the northwest and the Central Range to the southwest (Figure 1b). As the western extension of the Okinawa Trough, the Ilan Basin is sitting in an extension environment bounded by a series of normal faults (Hou et al., 2009; Kang et al., 2015). While field surveys of the normal faults have been limited due to the thick sediments in the area, a series of basement faults beneath the Ilan Basin were identified in seismic reflection profiles (Chiang, 1976). Major faults in this region mainly trend in NE-SW to E-W directions, including the Yaichein Fault, Ilan Fault, Kengssu Fault in the northern half of the basin and the Choshui Fault, Sansing Fault in the southern half, where the Choshui Fault is considered as the extension of Lishan Fault.

Cross-section D-D′ cuts across the Ilan Basin in a N-S direction revealing its clear basement geometry where the deepest part is located slight north of the basin center (Figures 8b and 10d). This geometry is consistent with previous studies based on active source seismic exploration (Chiang, 1976) and Sp converted phase analysis (Chang et al., 2010). These early studies suggested the maximum depth of the basin floor to be ∼1200 m (Chang et al., 2010). At ∼1200 m depth, our model has a Vs ∼2000 m/s at the deepest part of the basin, which is faster than the 1500 m/s basin floor velocity beneath the Taipei Basin. We suggest this velocity difference is reflecting different lithologies and ages of the rock below these two basins, as evident by the geological units surrounded these two basins.

On the southern end of the DD′ cross-section (also the southeastern end of the CC′), a low velocity anomaly is observed at depths below ∼4 km beneath the southern Ilan Basin (Figures 10d and 8d), an area with active geothermal and seismic activities. In 2005, a moderate earthquake doublet occurred in this low velocity region beneath the southern Ilan Basin and caused intensive shaking across the basin (Lai et al., 2009). Previous studies have suggested that a dyke intrusion might be the cause behind the earthquake doublet and the abnormally high thermal gradient observed in the area (Lai et al., 2009; Shen et al., 2020; Tong et al., 2008). The slow anomaly found in our profile D-D′ may reflect a fractured zone with geothermal fluids associated with this dyke feature zone.

5. Conclusions

In this study, we demonstrate that a detailed regional crustal velocity model can be constructed using multi-component noise cross-correlations and a temporary seismic array with ∼5 km station spacing. More specifically, we construct the first high-resolution regional 3-D shear velocity model of Northern Taiwan by analyzing continuous noise signals recorded by the dense broadband FA. We extract robust Rayleigh wave signals from multi-component noise cross-correlations and obtain high quality Rayleigh wave phase velocity and H/V ratio measurements across the array. Utilizing the complementary sensitivity of the two types of measurements, our inverted model reveals detailed shallow crustal structures that are well correlated with surface geological features and provides new constraints on the geometry of active sedimentary basins and fault systems in the area.

Compared to earlier studies in the region using earthquake body waves and active source profiles, the new 3D model presented in this study is more comprehensive and covers the entire Northern Taiwan with more or less even spatial resolution. The addition of Rayleigh wave H/V ratio measurements to the conventional dispersion based ambient noise tomography also significantly improves the sensitivity to near surface velocity structure and allows detailed shallow crustal structure to be resolved with sub-kilometer depth resolution. Our model illuminates in greater detail the half-graben geometry of the Taipei and Ilan Basins, possible magmatic structures beneath the Tatun Volcano and Southern Ilan Plain, geometrical relationships of Shanchiao Fault and a rifted basin mantled by the TVG, and the stepwise velocity increases related to imbrication of thrust faults (e.g., Hsintien Fault and Chuchih Fault) across the Hsuehshan Range.

High-resolution imaging of such shallow geological structures bridges the gap between the geological and geophysical observations that often imply different scale structures. The finer features resolved in the new model may assess and provide clearer understanding to the post-collisional tectonic processes and potential sources of seismic hazards in Northern Taiwan. On the trend of large-N arrays nowadays, deploying denser geophone arrays could further increase the resolution to examine more local structures (Wang et al., 2019). Moreover, investigating anisotropy using directional dependent surface wave measurements (Lin et al., 2011) and Rayleigh-Love discrepancy (Moschetti et al., 2010), extending the resolution from upper crust to the entire lithosphere by integrating long-period teleseismic surface wave data (Yang et al., 2008) and complimentary body wave data (Fang et al., 2016) will be the directions of future studies.

Data Availability Statement

All processed cross-correlation functions are made to open access in a Harvard Dataverse reciprocity (https://doi.org/10.7910/DVN/E0SVML).

References

Bao, F., Li, Z., Tian, B., Wang, L., & Tu, G. (2019). Sediment thickness variations of the Tangshan fault zone in North China from a dense seismic array and microtremor survey. *Journal of Asian Earth Sciences*, *185*, 104045. https://doi.org/10.1016/j.jseaes.2019.104045

Bensen, G. D., Ritzwoller, M. H., Barmin, M. P., Levshin, A. L., Lin, F., Moschetti, M. P., et al. (2007). Processing seismic ambient noise data to obtain reliable broad-band surface wave dispersion measurements. *Geophysical Journal International*, *169*(3), 1239–1260. https://doi.org/10.1111/j.1365-246x.2007.03374.x

Berg, E. M., Lin, F.-C., Allam, A., Qiu, H., Shen, W., & Ben-Zion, Y. (2018). Tomography of Southern California via Bayesian joint inversion of Rayleigh wave ellipticity and phase velocity from ambient noise cross-correlations. *Journal of Geophysical Research: Solid Earth*, *123*(11), 9933–9949. https://doi.org/10.1029/2018jb016269

Berg, E. M., Lin, F. C., Allam, A., Schulte-Pelkum, V., Ward, K. M., & Shen, W. (2020). Shear velocity model of Alaska via joint inversion of Rayleigh wave ellipticity, phase velocities, and receiver functions across the Alaska transportable array. *Journal of Geophysical Research: Solid Earth*, *125*(2), e2019JB018582. https://doi.org/10.1029/2019jb018582

Brocher, T. M. (2005). Empirical relations between elastic wave speeds and density in the Earth's crust. *Bulletin of the Seismological Society of America*, *95*(6), 2081–2092. https://doi.org/10.1785/0120050077

Chang, C. H., Lin, T. L., Wu, Y. M., & Chang, W. Y. (2010). Basement imaging using Sp converted phases from a dense strong-motion array in Lan-Yang Plain, Taiwan. *Bulletin of the Seismological Society of America*, *100*(3), 1363–1369. https://doi.org/10.1785/0120090305

Chang, Y. J., & Lin, C. W. (2015). A Study on structural characteristics of the Chuchih Fault of Northern Taiwan: Central geological survey. *MOEA*, *28*, 29–54. (in Chinese).

Chen, C. T., Hu, J. C., Lu, C. Y., Lee, J. C., & Chan, Y. C. (2007). Thirty-year land elevation change from subsidence to uplift following the termination of groundwater pumping and its geological implications in the Metropolitan Taipei Basin, Northern Taiwan. *Engineering Geology*, *95*(1–2), 30–47. https://doi.org/10.1016/j.enggeo.2007.09.001

Chen, C.-T., Lee, J.-C., Chan, Y.-C., Lu, C.-Y., & Teng, L. S.-Y. (2014). Elucidating the geometry of the active Shanchiao Fault in the Taipei metropolis, Northern Taiwan, and the reactivation relationship with pre-existing orogen structures. *Tectonics*, *33*(12), 2400–2418. https://doi.org/10.1002/2013tc003502

Chen, C.-T., Wen, K.-L., & Huang, J.-Y. (2020). Source location-dependency site response in the Taipei Basin of Taiwan by using HVSR analysis. *Journal of Asian Earth Sciences*, *191*, 104223. https://doi.org/10.1016/j.jseaes.2019.104223

Chen, K. C. (2003). Strong ground motion and damage in the Taipei basin from the Moho reflected seismic waves during the March 31, 2002, Hualien, Taiwan earthquake. *Geophysical Research Letters*, *30*(11). https://doi.org/10.1029/2003gl017193

Chiang, S. C. (1976). A seismic refraction prospecting of the Ilan Plain. *Mining Tech*, *14*, 215–221.

Chu, M.-F., Lai, Y.-M., Li, Q., Chen, W.-S., Song, S.-R., Lee, H.-Y., & Lin, T.-H. (2018). Magmatic pulses of the Tatun Volcano Group, Northern Taiwan, revisited: Constraints from zircon U-Pb ages and Hf isotopes. *Journal of Asian Earth Sciences*, *167*, 209–217. https://doi.org/10.1016/j.jseaes.2018.05.028

Fang, H., Zhang, H., Yao, H., Allam, A., Zigone, D., Ben-Zion, Y., et al. (2016). A new algorithm for three-dimensional joint inversion of body wave and surface wave data and its application to the Southern California plate boundary region. *Journal Of Geophysical Research: Solid Earth*, *121*, 3557–3569. https://doi.org/10.1002/2015JB012702

Feng, L., Liu, C., & Ritzwoller, M. H. (2020). Azimuthal anisotropy of the crust and uppermost mantle beneath Alaska. *Journal of Geophysical Research: Solid Earth*, *125*(12), e2020JB020076. https://doi.org/10.1029/2020jb020076

Ho, C. S. (1986). A synthesis of the geologic evolution of Taiwan. *Tectonophysics*, *125*(1–3), 1–16. https://doi.org/10.1016/0040-1951(86)90004-1

Hou, C. S., Hu, J. C., Ching, K. E., Chen, C. L., Cheng, L. W., et al. (2009). The crustal deformation of the Ilan Plain acted as a westernmost extension of the Okinawa Trough. *Tectonophysics*, *466*(3–4), 344–355. https://doi.org/10.1016/j.tecto.2007.11.022

Huang, C. S., Chang, H. C., Lee, Y. H., & Lin, C. T. (1994). The Hsintien Fault and Related Features in the Taipei Suburb Area. *Ti-Chih, 14*, 1–18. (in Chinese).

Huang, H. H., Shyu, J. B. H., Wu, Y. M., Chang, C. H., & Chen, Y. G. (2012). Seismotectonics of northeastern Taiwan: kinematics of the transition from waning collision to subduction and postcollisional extension. *Journal of Geophysical Research: Solid Earth*, *117*(B1). https://doi.org/10.1029/2011jb008852

Huang, H.-H., Wu, E.-S., Lin, C.-H., Ko, J. Y., Shih, M.-H., & Koulakov, I. (2021). *Unveiling Tatun volcanic plumbing structure induced by post-collisional extension of Taiwan mountain belt*. Scientific Reports. in press. https://doi.org/10.5194/amt-2020-201-ac2

Huang, H.-H., Wu, Y.-M., Song, X., Chang, C.-H., Lee, S.-J., Chang, T.-M., & Hsieh, H.-H. (2014). Joint Vp and Vs tomography of Taiwan: Implications for subduction-collision orogeny. *Earth and Planetary Science Letters*, *392*, 177–191. https://doi.org/10.1016/j.epsl.2014.02.026

Huang, S.-Y., Rubin, C. M., Chen, Y.-G., & Liu, H.-C. (2007). Prehistoric earthquakes along the Shanchiao fault, Taipei Basin, northern Taiwan. *Journal of Asian Earth Sciences*, *31*(3), 265–276. https://doi.org/10.1016/j.jseaes.2006.07.025

Huang, T. Y., Gung, Y., Kuo, B. Y., Chiao, L. Y., & Chen, Y. N. (2015). Layered deformation in the Taiwan orogen. *Science*, *349*(6249), 720–723. https://doi.org/10.1126/science.aab1879

Huang, T. Y., Gung, Y., Liang, W. T., Chiao, L. Y., & Teng, L. S. (2012). Broad-band Rayleigh wave tomography of Taiwan and its implications on gravity anomalies. *Geophysical Research Letters*, *39*(5). https://doi.org/10.1029/2011gl050727

Huang, Y.-C., Yao, H., Huang, B.-S., van der Hilst, R. D., Wen, K.-L., Huang, W.-G., & Chen, C.-H. (2010). Phase velocity variation at periods of 0.5-3 seconds in the Taipei Basin of Taiwan from correlation of ambient Seismic noise. *Bulletin of the Seismological Society of America*, *100*(5A), 2250–2263. https://doi.org/10.1785/0120090319

Institute of Earth Sciences, A. S. (1996). *Broadband array in Taiwan for seismology*. Institute of Earth Sciences, Academia Sinica, Taiwan. https://doi.org/10.7914/SN/TW

Institute of Earth Sciences, A. S. (2017). *Formosa array*. Institute of Earth Sciences, Academia Sinica, Taiwan. https://doi.org/10.7914/SN/FM

Jaxybulatov, K., Shapiro, N. M., Koulakov, I., Mordret, A., Landès, M., & Sens-Schönfelder, C. (2014). A large magmatic sill complex beneath the Toba caldera. *Science*, *346*(6209), 617–619. https://doi.org/10.1126/science.1258582

Jiang, C., Schmandt, B., Farrell, J., Lin, F.-C., & Ward, K. M. (2018). Seismically anisotropic magma reservoirs underlying silicic calderas. *Geology*, *46*(8), 727–730. https://doi.org/10.1130/g45104.1

Kang, C.-C., Chang, C.-P., Siame, L., & Lee, J.-C. (2015). Present-day surface deformation and tectonic insights of the extensional Ilan Plain, NE Taiwan. *Journal of Asian Earth Sciences*, *105*, 408–417. https://doi.org/10.1016/j.jseaes.2015.02.013

Kuo-Chen, H., Wu, F. T., & Roecker, S. W. (2012). Three-dimensional P velocity structures of the lithosphere beneath Taiwan from the analysis of TAIGER and related seismic data sets. *Journal of Geophysical Research: Solid Earth*, *117*(B6).

Lai, K.-Y., Chen, Y.-G., Wu, Y.-M., Avouac, J.-P., Kuo, Y.-T., Wang, Y., et al. (2009). The 2005 Ilan earthquake doublet and seismic crisis in northeastern Taiwan: Evidence for dyke intrusion associated with on-land propagation of the Okinawa Trough. *Geophysical Journal International*, *179*(2), 678–686. https://doi.org/10.1111/j.1365-246x.2009.04307.x

Lee, C. S., Shor, G. G., Jr, Bibee, L. D., Lu, R. S., & Hilde, T. W. (1980). Okinawa Trough: Origin of a back-arc basin. *Marine Geology*, *35*(1–3), 219–241. https://doi.org/10.1016/0025-3227(80)90032-8

Lee, J. C., Angelier, J., & Chu, H. T. (1997). Polyphase history and kinematics of a complex major fault zone in the northern Taiwan mountain belt: The Lishan fault. *Tectonophysics*, *274*(1–3), 97–115. https://doi.org/10.1016/s0040-1951(96)00300-9

Lee, S.-J., Chen, H.-W., Liu, Q., Komatitsch, D., Huang, B.-S., & Tromp, J. (2008). Three-dimensional simulations of seismic-wave propagation in the Taipei basin with realistic topography based upon the spectral-element method. *Bulletin of the Seismological Society of America*, *98*(1), 253–264. https://doi.org/10.1785/0120070033

Lee, S.-J., Chen, H.-W., & Ma, K.-F. (2007). Strong ground motion simulation of the 1999 Chi-Chi, Taiwan earthquake from a realistic three-dimensional source and crustal structure. *Journal of Geophysical Research*, *112*, B06307. https://doi.org/10.1029/2006JB004615

Letouzey, J., & Kimura, M. (1986). The Okinawa Trough: Genesis of a back-arc basin developing along a continental margin. *Tectonophysics*, *125*(1–3), 209–230. https://doi.org/10.1016/0040-1951(86)90015-6

Li, G., Chen, H., Niu, F., Guo, Z., Yang, Y., & Xie, J. (2016). Measurement of Rayleigh wave ellipticity and its application to the joint inversion of high-resolution S wave velocity structure beneath northeast China. *Journal Of Geophysical Research: Solid Earth*, *121*(2), 864–880. https://doi.org/10.1002/2015jb012459

Lin, A. T., & Watts, A. B. (2002). Origin of the West Taiwan basin by orogenic loading and flexure of a rifted continental margin. *Journal of Geophysical Research: Solid Earth*, *107*(B9). ETG-2. https://doi.org/10.1029/2001jb000669

Lin, C. H. (2016). Evidence for a magma reservoir beneath the Taipei metropolis of Taiwan from both S-wave shadows and P-wave delays. *Scientific Reports*, *6*, 39500.

Lin, F.-C., Moschetti, M. P., & Ritzwoller, M. H. (2008). Surface wave tomography of the western United States from ambient seismic noise: Rayleigh and Love wave phase velocity maps. *Geophysical Journal International*, *173*(1), 281–298. https://doi.org/10.1111/j.1365-246x.2008.03720.x

Lin, F.-C., Ritzwoller, M. H., & Snieder, R. (2009). Eikonal tomography: surface wave tomography by phase front tracking across a regional broad-band seismic array. *Geophysical Journal International*, *177*(3), 1091–1110. https://doi.org/10.1111/j.1365-246x.2009.04105.x

Lin, F.-C., Ritzwoller, M. H., Yang, Y., Moschetti, M. P., & Fouch, M. J. (2011). Complex and variable crustal and uppermost mantle seismic anisotropy in the western United States. *Nature Geoscience*, *4*(1), 55–61. https://doi.org/10.1038/ngeo1036

Lin, F.-C., Tsai, V. C., & Schmandt, B. (2014). 3-D crustal structure of the western United States: Application of Rayleigh-wave ellipticity extracted from noise cross-correlations. *Geophysical Journal International*, *198*(2), 656–670. https://doi.org/10.1093/gji/ggu160

Liu, C. S., Huang, I. L., & Teng, L. S. (1997). Structural features off southwestern Taiwan. *Marine Geology*, *137*(3–4), 305–319. https://doi.org/10.1016/s0025-3227(96)00093-x

McIntosh, K., Nakamura, Y., Wang, T. K., Shih, R. C., Chen, A., & Liu, C. S. (2005). Crustal-scale seismic profiles across Taiwan and the Western Philippine Sea. *Tectonophysics*, *401*(1–2), 23–54. https://doi.org/10.1016/j.tecto.2005.02.015

Moschetti, M. P., Ritzwoller, M. H., Lin, F., & Yang, Y. (2010). Seismic evidence for widespread western-US deep-crustal deformation caused by extension. *Nature*, *464*(7290), 885–889. https://doi.org/10.1038/nature08951

Muir, J. B., & Tsai, V. C. (2017). Rayleigh-wave H/V via noise cross correlation in Southern California. *Bulletin of the Seismological Society of America*, *107*(5), 2021–2027. https://doi.org/10.1785/0120170051

Olsen, K. B. (2000). Site amplification in the Los Angeles basin from three-dimensional modeling of ground motion. *Bulletin of the Seismological Society of America*, *90*(6B), S77–S94. https://doi.org/10.1785/0120000506

Roy, C., & Romanowicz, B. A. (2017). On the implications of a priori constraints in transdimensional Bayesian inversion for continental lithospheric layering. *Journal of Geophysical Research: Solid Earth*, *122*(12), 10–118. https://doi.org/10.1002/2017jb014968

Shapiro, N. M., Campillo, M., Stehly, L., & Ritzwoller, M. H. (2005). High-resolution surface-wave tomography from ambient seismic noise. *Science*, *307*(5715), 1615–1618. https://doi.org/10.1126/science.1108339

Shen, T.-T., Liu, T.-K., Huang, S.-Y., Hsieh, P.-S., & Wu, C.-Y. (2020). Post-collisional exhumation and geotherm pattern in northern Tananao Complex, Northeastern Taiwan. *Terrestrial, Atmospheric and Oceanic Sciences*, *31*, 369–381. https://doi.org/10.3319/TAO.2019.04.06.01

Shen, W., & Ritzwoller, M. H. (2016). Crustal and uppermost mantle structure beneath the United States. *Journal Of Geophysical Research: Solid Earth*, *121*(6), 4306–4342. https://doi.org/10.1002/2016jb012887

Shen, W., Ritzwoller, M. H., Schulte-Pelkum, V., & Lin, F.-C. (2013). Joint inversion of surface wave dispersion and receiver functions: A Bayesian Monte-Carlo approach. *Geophysical Journal International*, *192*(2), 807–836. https://doi.org/10.1093/gji/ggs050

Shyu, J. B. H., Chuang, Y. R., Chen, Y. L., Lee, Y. R., & Cheng, C. T. (2016). A new on-land Seismogenic structure source database from the Taiwan Earthquake Model (TEM) project for Seismic hazard analysis of Taiwan. *Terrestrial, Atmospheric and Oceanic Sciences*, *27*(3). https://doi.org/10.3319/tao.2015.11.27.02(tem)

Shyu, J. B. H., Sieh, K., Chen, Y.-G., & Liu, C.-S. (2005). Neotectonic architecture of Taiwan and its implications for future large earthquakes. *Journal of Geophysical ResearchAtmospheres*, *110*, B08402. https://doi.org/10.1029/2004JB003251

Smith, K., & Tape, C. (2019). Seismic noise in central Alaska and influences from rivers, wind, and sedimentary basins. *Journal Of Geophysical Research: Solid Earth*, *124*(11), 11678–11704. https://doi.org/10.1029/2019jb017695

Song, S. R. (2000). The Tatun volcano group is active or extinct?. *Journal Of Geological Society Of China*, *43*, 521–534.

Spica, Z., Perton, M., Nakata, N., Liu, X., & Beroza, G. C. (2018). Shallow VS imaging of the Groningen Area from joint inversion of multimode surface waves and H/V spectral ratios. *Surface Waves and H/V Spectral Ratios*, *89*(5), 1720–1729. https://doi.org/10.1785/0220180060

Suppe, J. (1980). A retrodeformable cross section of northern Taiwan. In *Proceedings of the Geological Society of China, 23*, 46–55.

Suppe, J. (1981). Mechanics of mountain building and metamorphism in Taiwan. *Memoir of the Geological Society of China*, *4*(6), 67–89.

Suppe, J., Schaer, J. P., & Rodgers, J. (1987). Chapter 15. The active Taiwan mountain belt. In *The Anatomy of Mountain Ranges*, 277–294. Princeton, NJ: Princeton University Press. https://doi.org/10.1515/9781400858644.277

Tanimoto, T., & Rivera, L. (2008). The ZH ratio method for long-period seismic data: Sensitivity kernels and observational techniques. *Geophysical Journal International*, *172*, 187–198. https://doi.org/10.1111/j.1365-246X.2007.03609.x

Teng, L. S. (1996). Extensional collapse of the northern Taiwan mountain belt. *Geology*, *24*(10), 949–952. https://doi.org/10.1130/0091-7613(1996)024<0949:ecotnt>2.3.co;2

Teng, L. S., Lee, C. T., Peng, C. H., Chen, W. F., & Chu, C. J. (2001). Origin and geological evolution of the Taipei Basin, Northern Taiwan. *Western Pacific Earth Sciences*, *1*(2), 115–142.

Tong, L. T., Ouyang, S., Guo, T. R., Lee, C. R., Hu, K. H., Lee, C. L., & Wang, C. J. (2008). Insight into the geothermal structure in Chingshui, Ilan, Taiwan. *Terrestrial, Atmospheric and Oceanic Sciences*, *19*(4). https://doi.org/10.3319/tao.2008.19.4.413(t)

Tsai, C.-C., Yeh, Y.-T., Wen, K.-L., Cheng, S.-N., & Kao, M.-H. (1986). The Hualien earthquake of May 20, 1986: Strong ground motion data and response spectra. *Bulletin of the Institute of Earth Sciences, Academia Sinica*, *6*, 29–64.

Wang, C.-Y., Lee, Y.-H., Ger, M.-L., & Chen, Y.-L. (2004). Investigating Subsurface Structures and P- and S-wave Velocities in the Taipei Basin. *Terrestrial, Atmospheric and Oceanic Sciences*, *15*, 609–628. https://doi.org/10.3319/tao.2004.15.4.609(t)

Wang, K., Lu, L., Maupin, V., Ding, Z., Zheng, C., & Zhong, S. (2020). Surface wave tomography of Northeastern Tibetan Plateau using beamforming of seismic noise at a dense array. *Journal of Geophysical Research: Solid Earth*, *125*(4), e2019JB018416. https://doi.org/10.1029/2019jb018416

Wang, W. H., & Chen, C. H. (1990). The volcanology and fission track age dating of pyroclastic deposits in Tatun Volcanico group, Northern Taiwan. *Yánjiū bàogào-Guólì Táiwān dàxué. Lǐxuéyuàn Dìzhìxué Xì*. Acta Geologica Taiwanica (28), 1–30.

Wang, Y., Allam, A., & Lin, F.-C. (2019). Imaging the fault damage zone of the San Jacinto Fault near Anza with ambient noise tomography using a dense nodal array. *Geophysical Research Letters*, *46*. https://doi.org/10.1029/2019gl084835

Wu, Y. M., Chang, C. H., Zhao, L., Shyu, J. B. H., Chen, Y. G., Sieh, K., & Avouac, J. P. (2007). Seismic tomography of Taiwan: Improved constraints from a dense network of strong motion stations. *Journal of Geophysical Research: Solid Earth*, *112*(B8). https://doi.org/10.1029/2007jb004983

Yang, Y., Ritzwoller, M. H., Lin, F.-C., Moschetti, M. P., & Shapiro, N. M. (2008). Structure of the crust and uppermost mantle beneath the western United States revealed by ambient noise and earthquake tomography. *Journal of Geophysical Research*, *113*, B12310. https://doi.org/10.1029/2008JB005833

Yao, H., Van Der Hilst, R. D., & Montagner, J. P. (2010). Heterogeneity and anisotropy of the lithosphere of SE Tibet from surface wave array tomography. *Journal of Geophysical Research: Solid Earth*, *115*(B12). https://doi.org/10.1029/2009jb007142